ORIGINAL PAPER

Heterogeneous Swelling of an Isotropically Compacted Bentonite-Based Material: Experimental Observations and Modelling

Anne-Catherine Dieudonné[1] · Claude Gatabin[2] · Wissem Dridi[2] · Jean Talandier[3] · Frédéric Collin[4] · Robert Charlier[4]

Abstract

This paper presents a comprehensive investigation of the swelling behaviour of a compacted bentonite–sand mixture subjected to hydration under constant volume conditions. Contrary to previous studies, the tested sample was isotropically compacted before being hydrated under constant volume conditions until full saturation was reached. The total axial pressure, total radial pressures at four different heights of the sample, and injected water volume were recorded over time. The experimental data reveal a complex and non-uniform evolution of the axial and radial stresses over time, as well as anisotropy of the total stresses, which persist at the saturated equilibrated state. To gain further insights, a numerical analysis was performed using an advanced hydromechanical framework for partially saturated porous media, accounting for the evolving microstructure of the material. The complex evolution of the total axial and radial pressures with time is attributed to the advancing hydration and swelling front in the sample, along with the development of irreversible strains. The good agreement between the numerical results and the experimental data enables validation of the developed framework. Implications for engineered barriers in deep geological disposal of radioactive waste are discussed.

Highlights

- The swelling behaviour of an isotropically compacted bentonite-based material under constant-volume conditions is investigated.
- Hydration of the sample generates stress heterogeneity and anisotropy, which persist at the saturated equilibrated state.
- Numerical modelling shows that the complex evolution of the total axial and radial pressures can be attributed to the advancing hydration and swelling front in the sample, along with the development of irreversible strains.
- The relationship between the local dry density and the radial stress seems to follow the global dry density-swelling pressure trend determined on small-scale samples.

✉ Anne-Catherine Dieudonné
a.a.m.dieudonne@tudelft.nl

[1] Faculty of Civil Engineering and Geosciences, Delft University of Technology, Delft, The Netherlands

[2] Den-Service d'Etude du Comportement des Radionucléides (SECR), CEA, Université de Paris-Saclay, 91191 Gif-Sur-Yvette, France

[3] French National Radioactive Waste Management Agency (Andra), Châtenay-Malabry Cedex, France

[4] Urban and Environmental Engineering Research Unit, University of Liege, Liege, Belgium

1 Introduction

The swelling pressure developed by an engineered barrier upon saturation is a key aspect of the design and safety assessment of geological disposal facilities for radioactive waste. The swelling pressure should be sufficiently high to create a good seal and close the fractures of the excavation damaged zone, but it should not exceed the natural stress of the geological formation. In that case, it could indeed damage the host rock and create preferential pathways for

radionuclides migration (Bucher and Müller-Vonmoos 1989; Pusch 1992; Sellin and Leupin 2013).

Three types of laboratory tests are typically performed to characterise the swelling behaviour of bentonites (Brackley 1973; Sridharan et al. 1986): swelling pressure tests (Lloret et al. 2003; Agus and Schanz 2008; Villar and Lloret 2008; Gatabin et al. 2016; Middelhoff et al. 2020), swell-consolidation tests (Cui et al. 2002; Rao and Thyagaraj 2007) and swell-under-load tests (Cui et al. 2002; Lloret et al. 2003; Rao and Thyagaraj 2007; Villar and Lloret 2008). The three experimental techniques, described in ASTM D4546 (2014), provide three estimations of the swelling pressure. The swelling pressures determined by swell-consolidation tests have been found to be larger than those determined by swell-under-load tests (Brackley 1973; Sridharan et al. 1986; Cui et al. 2002; Wang et al. 2012), while swelling pressure tests give intermediate values (Sridharan et al. 1986). The difference between the different values has been attributed to stress path dependency of the mechanical behaviour of bentonites (Sridharan et al. 1986; Villar and Lloret 2008).

The above-mentioned laboratory tests have generally been performed on small (10- or 20-mm high) samples, mainly due to cell availability and time reasons. The very low permeabilities of compacted bentonites yield indeed very long saturation times. Accordingly, limited monitoring of the samples is possible, and the swelling capacity is characterised by a single value, namely, the external axial stress, implicitly assuming the processes to be isotropic and homogeneous. In other words, the tests are considered as being element tests. Only in rare cases, the radial swelling stress was measured in addition to the axial component (Alonso et al. 2011; Lee et al. 2012; Saba et al. 2014a; Rawat et al. 2019, 2020; Bernachy-Barbe 2021). However, at least two factors are likely to contribute to non-homogeneous swelling of bentonite samples: the sample compaction procedure, which is generally uniaxial, hence anisotropic, and the hydration procedure.

Tang and Cui (2010) showed that the free-swelling hydration of isotropically compacted bentonite was isotropic, while uniaxially compacted bentonite displayed anisotropic swelling. In that case, the axial strain was significantly higher than the radial strain. The same observation was made by Denis (1991) on Redhill smectite and by Gatabin et al. (2016) on a mixture of bentonite and sand. The swelling anisotropy has been attributed to the uniaxial compaction process used for the preparation of the samples, which induces a preferential orientation of the clay particles in the horizontal plane (Hicher et al. 2000; Sato and Suzuki 2003; Voltolini et al. 2009). Anisotropy of the mechanical behaviour of uniaxially compacted samples was also evidenced by Cui et al. (2002) on isotropic loading tests performed on isotropically and anisotropically compacted samples. Larger compression strains were observed along the virgin

compression line on the anisotropically compacted samples, while the unloading line followed a slope close to the one of the isotropically compacted samples. Cui et al. (2002) attributed this behaviour to a progressive reorganisation of the material structure towards a more isotropic structure.

On the other hand, Saba et al. (2014b) emphasised the inhomogeneous swelling of larger, uniaxially compacted, bentonite samples (60- and 120-mm high) hydrated from one end. The authors showed that the radial stress developed upon hydration was significantly lower than the axial stress and varied along the sample height. The isochoric hydration of an anisotropically compacted sample thus leads to an anisotropic state of stress. Similar conclusions were drawn from laboratory tests investigating the closure of technological voids (see, among others, Wang et al. 2013b; Harrington et al. 2020; Zeng et al. 2020, 2022; Villar et al. 2023). However, the relative contributions of the anisotropic material behaviour and of the hydration process on the induced anisotropic state of stress has not been assessed.

This paper sheds the light on the anisotropic and heterogeneous swelling of a compacted bentonite-based material due to progressive hydration. For this purpose, the behaviour of an isotropically compacted sample subjected to water infiltration was investigated. The axial and radial total stresses at different distances from the wetting end, along with the injected water volume, were monitored until reaching steady-state conditions. Numerical simulations, using a fully coupled hydromechanical framework, were performed to support test interpretation. In particular, the Barcelona Basic Model (Alonso et al. 1990) and a classic flow law for partially saturated porous media were extended to account for the important water retention capacity and specific double-structure of compacted bentonites. Implications for the disposal of radioactive waste are finally discussed.

2 Infiltration Test

2.1 Material Properties and Sample Preparation

The material used in this study was a mixture of Wyoming MX-80 bentonite (commercially known as WH2 Gelclay) and quartz sand with a respective proportion of 70/30 in dry mass. MX-80 bentonite contains 92% of montmorillonite and other minerals including quartz and feldspars (Tang et al. 2008). The cation exchange capacity (CEC) is 76 meq/100 g and the major exchangeable cation is Na^+ (83%) (Wang et al. 2013a). To facilitate a homogeneous mixture and compaction, the grain size distributions (obtained by dry sieving) were similar for both materials and in the range of 0.2–2 mm. The initial gravimetric water content of the bentonite/sand mixture was 12.4%.

The sample was compacted by cold isostatic pressing to reach a high degree of homogeneity. The compaction pressure was slowly increased to a value of 30 MPa, corresponding to a final dry density of 1.78 Mg/m^3. This dry density was selected to reach the estimated in situ dry density of the bentonite plug in the PGZ2 experiment performed by the French National Radioactive Waste Management Agency (Andra) in the Meuse/Haute-Marne Underground Research Laboratory (de La Vaissière 2013). The core was then machined to a diameter of 120.0 mm and a height of 100.0 mm to fit the infiltration cell.

2.2 Experimental Setup

The infiltration test was performed under constant volume conditions using the experimental setup presented in Fig. 1. The bentonite plug was placed in a confining cell made of stainless steel and was sandwiched between two stainless steel porous discs with average pore diameter of 20 μm. The upper disc allowed fluid exchanges with the ambient controlled atmosphere, while the lower one was used for water supply. The piston was then placed, and the whole assembly was fixed in a high-rigidity frame. An external linear variable differential transducer was installed to record any displacement and check the constant-volume conditions. Finally, a vertical preload of 0.2 MPa was applied to ensure good contact between the materials.

To follow the hydromechanical state of the sample during hydration, the total vertical pressure and the injected water volume were recorded over time. The load cell used to monitor the vertical total pressure had a maximum loading capacity of 18 MPa with an accuracy of 0.9 kPa. Finally, the cell was equipped with four total radial pressure sensors, named PT1 to PT4, and placed at different heights of the sample. These sensors were piezoresistive flush diaphragm pressure transducers configured in a Wheatstone bridge circuit. They allowed a measurement range of 0–10 MPa with a sensitivity of 0.9 mV/MPa. The positions of the total radial pressure sensors are given in Table 1.

2.3 Experimental Protocol

The water used for hydration was a synthetic water representative of the site of Bure, France. Its chemical composition is given in Table 2. Its salinity is 0.26% (0.058 M) and its pH is 7.7. Hydration was performed from the bottom end at a water pressure of 0.11 MPa for 1 year. During that time, the flushing line on the top was kept open to ensure evacuation of air during the hydration process. Then, a water pressure of 0.5 MPa was applied on the upper face of the sample to ensure full saturation of the sample. This pressure was maintained during 2 months. The experiment
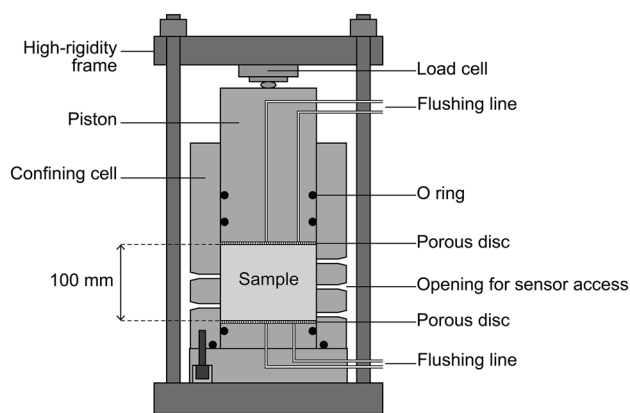

Fig. 1 Schematic representation of the experimental setup

Table 1 Position of the total radial pressure sensors. Height is measured from bottom (injection) end of the sample

Reference	Angle (°)	Height (mm)	Representation
PT1	0	12.5	
PT2	180	37.5	
PT3	270	50	
PT4	90	75	

Table 2 Composition of the synthetic water used in the infiltration test

Compound	Concentration (mmol/L)
Cl$^-$	39.61
Na$^+$	19.86
K$^+$	1.03
Ca^{2+}	7.36
Mg^{2+}	6.67
SO$_4^{2-}$	3.00
Ag$^+$	10^{-3}
pH	7.7
M	0.058
Salinity (%)	0.26

was performed in a climate room with a constant temperature of 20 °C.

3 Theoretical Formulation

To gain insight into the behaviour of the sample upon hydration, a fully coupled hydro-mechanical simulation of the test was performed. The finite element code Lagamine was used (Charlier 1987).

The balance equations are obtained for a mixture composed of three species, namely, mineral, water and air, distributed in three phases, namely, solid, liquid and gas. Accordingly, the kinematics of the porous medium is described by its displacement field u, liquid pressure field, which is equivalent to the water pressure field u_w and gas pressure field u_g. In the present formulation, it is assumed that the mineral species and the solid phase coincide. The liquid phase contains both water and dissolved air, while the gas phase is a perfect mixture of dry air and water vapour. According to Dalton's law, the total pressure of the gas phase is equal to the sum of the partial pressures of dry air and water vapour. This total gas pressure was fixed constant and equal to the atmospheric pressure throughout the simulation since the infiltration test was essentially performed under air-drained conditions (top flushing line open).

3.1 Balance Equations

The compositional approach (Panday and Corapcioglu 1989; Olivella et al. 1994; Collin et al. 2002) is adopted to establish the mass balance equations. It consists of balancing species rather than phases. For a given volume of mixture Ω, the mass balance of the solid phase reads

$$\frac{\partial}{\partial t}\left[\rho_s(1-\phi)\Omega\right] = 0 \tag{1}$$

where ρ_s is the density of the solids, ϕ is the porosity and t denotes time.

The water and air mass balance equations are expressed as

$$\underbrace{\frac{\partial}{\partial t}\left(\rho_w S_r \phi\right) + \nabla \cdot f_l^w}_{\text{Liquid water}} + \underbrace{\frac{\partial}{\partial t}\left[\rho_v\left(1 - S_r\right)\phi\right]}_{\text{Water vapour}} = Q^w \tag{2}$$

and

$$\underbrace{\frac{\partial}{\partial t}\left[\rho_a\left(1 - S_r\right)\phi\right]}_{\text{Dry air}} + \underbrace{\frac{\partial}{\partial t}\left(\rho_l^a S_r \phi\right) + \nabla \cdot f_l^a}_{\text{Dissolved air}} = Q^a \tag{3}$$

where ρ_w, ρ_v, ρ_a and ρ_l^a are the densities of liquid water, water vapour, dry air and dissolved air, respectively, S_r is the degree of saturation, f_l^w and f_l^a are the mass fluxes of liquid water and dissolved air, and Q^w and Q^a are water and air source terms.

The balance of momentum is expressed for the entire mixture. For quasi-static loading, the equation reduces to the equilibrium of stresses

$$\nabla \cdot \boldsymbol{\sigma_t} + \boldsymbol{b} = 0 \tag{4}$$

where $\boldsymbol{\sigma_t}$ is the total Cauchy stress tensor (with compressive stress taken as positive) and $\boldsymbol{b}$ is the body force vector.

3.2 Material Microstructure

Compacted bentonites exhibit a bimodal pore size distribution, which evolves along with mechanical and hydraulic loads (see Romero et al. 2011; Della Vecchia et al. 2015; Sun et al. 2019, among others). For such materials, pores can be classified into two main classes, namely, intra-aggregate pores (hereafter referred to as micro-pores) and inter-aggregate pores (hereafter referred to as macro-pores), such that

$$e = e_m + e_M \tag{5}$$

where e is the (total) void ratio, e_m is the microstructural void ratio (micro-pores volume over solid volume) and e_M is the macrostructural void ratio (macro-pores volume over solid volume). e_m is assumed to evolve with the water ratio (volume of water over solid volume), e_w, according to the law proposed by Dieudonné et al. (2013)

$$e_m = \beta_0 e_w^2 + \beta_1 e_w + e_{m0} \tag{6}$$

where e_{m0} is the microstructural void ratio for the dry material ($e_w = 0$) and β_0 and β_1 are parameters that quantify the swelling potential of the aggregates. These parameters were determined by analysing pore size distributions obtained by mercury intrusion porosity and using the method described by Della Vecchia et al. (2015) to differentiate between intra-aggregate and inter-aggregate pores.

3.3 Hydraulic Constitutive Equations

The advective flux of water is described by the generalised Darcy's law for partially saturated porous media. It is related to the water pressure u_w through

$$q_w = -\frac{K k_{rw}\left(S_r\right)}{\mu_w} \nabla u_w \tag{7}$$

where μ_w is the water dynamic viscosity, K is the water permeability in fully saturated conditions and k_{rw} is the relative

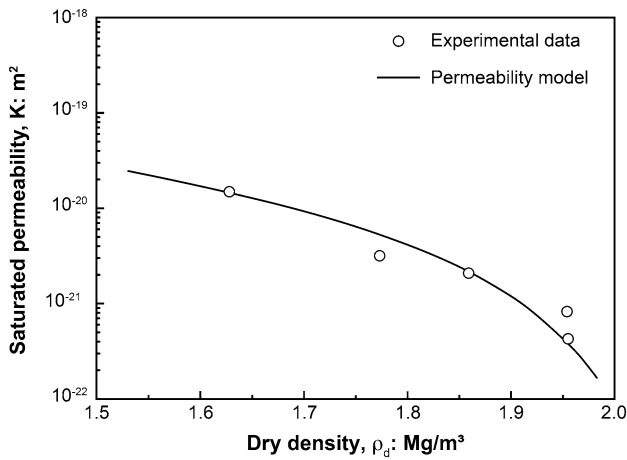**Fig. 2** Evolution of the water permeability of the MX-80 bentonite/sand mixture with dry density. Experimental data and model calibration
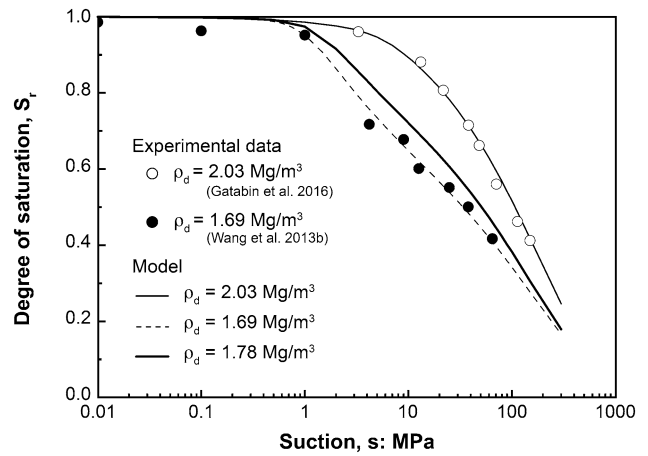

Fig. 3 Water retention curves of the mixture of MX-80 bentonite and sand. Experimental data (Wang et al. 2013b; Gatabin et al. 2016) and model calibration

permeability function, which is a function of the degree of saturation according to

$$k_{rw} = S_r^{n_k} \tag{8}$$

where n_k is a model parameter. n_k was determined equal to 3.4 by back-analysis of the water infiltration test performed by Wang et al. (2013b) on the same material (Dieudonné and Charlier 2017).

Advective flow is mainly controlled by the inter-aggregate porosity. Accordingly, the permeability is expressed as

$$K = K_0 \frac{e_M^2}{\left(1 - e_M\right)^{0.2}} \frac{\left(1 - e_{M0}\right)^{0.2}}{e_{M0}^2} \tag{9}$$

where K_0 is a reference permeability measured on a material with a macrostructural void ratio e_{M0}. Fig. 2 presents the model adopted together with experimental data from permeability tests performed on the same material compacted to different dry densities. A reference permeability of $K_0 = 2.5 10^{-20} m^2$ was adopted for a reference macrostructural void ratio $e_{M0} = 0.31$.

Finally, the water retention model of Dieudonné et al. (2017) is used

$$S_r = \frac{e_w}{e} = \frac{e_m}{e} \exp\left[-\left(C_{ads}s\right)^{n_{ads}}\right] + \frac{\left(e - e_m\right)}{e}\left\{1 + \left[\left(e - e_m\right)\frac{s}{A}\right]^n\right\}^{-m} \tag{10}$$

where C_{ads} and n_{ads} are material parameters controlling adsorption in the microstructure, and n, m and A are parameters controlling water retention in the macro-pores. These parameters were calibrated against water retention curves on the same material compacted to two dry densities (Dieudonné et al. 2017). The water retention curve corresponding to the initial dry density of the tested material is represented in Fig. 3.

The parameters of the microstructural and water retention models are presented in Table 3. Further details on their determination can be found in Dieudonné et al. (2017).

3.4 Mechanical Constitutive Equations

The Barcelona Basic Model (BBM) (Alonso et al. 1990) was extended to account for the important water retention capacity of bentonite. The BBM is formulated in terms of net stress and suction and, for null suction, the model coincides with the Modified Cam-Clay Model (Roscoe and Burland 1968). Accordingly, the model implicitly assumes that full saturation is achieved when suction is equal to zero and, along a wetting path, the model predicts elastic swelling strains due to suction decrease (and possibly irreversible pore collapse), regardless the saturation state of the material and until suction becomes null. However, bentonite-based materials are characterised by high air-occlusion values and, along a saturation path, the materials are saturated

	Microstructural model			Water retention model				
Table 3 Parameters of the hydraulic model for the mixture of MX-80 bentonite and sand	β_0	β_1	e_{m0}	C_{ads} (MPa^{-1})	n_{ads}	A (MPa)	n	m
	0.18	0.1	0.29	0.0053	0.79	0.2	3	0.15

before reaching zero suction. Agus et al. (2013) performed multi-step swelling pressure tests, where suction of bentonite specimens was reduced in a stepwise manner toward a zero value. The results show that there is a threshold suction below which the swelling pressure stabilises. The magnitude of the threshold suction is found to correspond to the air-occlusion value of the material. Swelling of compacted bentonites results indeed from the progressive intrusion of water within the interlayer space first (crystalline swelling), and then the interparticle space (osmotic swelling) (Jacinto et al. 2012). Consequently, along a wetting path, limited swelling is to be expected once the material is saturated, i.e., when suction is below the (current) material air-occlusion value.

Based on these observations and that comprehension of the swelling mechanisms, a threshold suction, below which the sample does not experience swelling strains, is introduced in the Barcelona Basic Model. It yields

$$\kappa_s = 0 \quad \text{for } s < s^* \tag{11}$$

where s^* is a threshold suction which may be assimilated to the air-occlusion value. However, the water retention curve proposed by Dieudonné et al. (2017) does not explicitly define the air-occlusion value. The criteria $s < s^*$ in Eq. (11) is, therefore, replaced by a criterion on the degree of saturation

$$\kappa_s = 0 \quad \text{for } S_r > S_r^* \tag{12}$$

where S_r^* is a threshold degree of saturation. For $S_r^* = 1$, the original formulation of the BBM is recovered. The complete formulation of the mechanical model is presented in Appendix A, together with its calibration against experimental data from controlled-suction oedometer tests. The parameters are given in Table 4.

4 Experimental Results, Analysis and Numerical Simulation

4.1 Injected Water Volume

Fig. 4 presents the evolution of the injected water volume over time. The experimental curve is characterised by a rapid increase in the injected water volume, corresponding to water filling of the dead volume (tubing) and saturation of the bottom porous disc. This volume was measured equal to 20 cm³ prior to the test and is used to correct the numerical
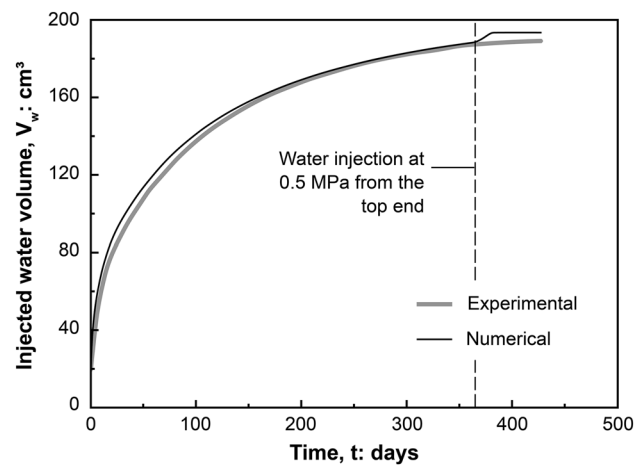
Fig. 4 Water volume injected from the bottom end. Comparison between experimental data and model predictions

curve. As observed in Fig. 4, the numerical model compares well with the experimental curve. As water injection proceeded, the injection rate decreased, both as a result of the smaller pressure gradient and of the decrease in the material permeability (due to the expansion of the clay aggregates, leading to a decrease in the macro-pore volume). The injected water volume reached 188.5 cm³ at the end of the first injection stage.

4.2 Typical Stress and Strain Paths Within the Sample

Before proceeding any further with the comparison between experimental data and numerical results, the stress and strain paths undergone by the sample are detailed. It is worth noting that, since hydration was not uniform within the sample, the followed stress and strain paths differed depending on the axial position of the point under consideration. Yet, one can identify common features and trends in these paths.

In the following, the paths followed by a point located at a height of 37.5 mm from the bottom end are thoroughly described. This point corresponds to the location of the total radial stress sensor PT2. The stress and strain paths followed by the considered point are represented in Figs. 5 and 6, respectively. In particular, the state of stress is described in terms of mean net stress p and deviatoric stress q (defined as the difference between the axial and radial stress). Let A be the initial state of the material at time $t = 0$. As hydration of the bentonite sample proceeded ($t > 0$), the stress and

Table 4 Parameters of the mechanical model for the mixture of MX-80 bentonite and sand

κ	κ_s	ν	$c(0)$ (MPa)	k	ϕ (°)	$\lambda(0)$	p_0^* (MPa)	p_c (MPa)	r	ω (MPa⁻¹)	S_r^*
0.025	0.073	0.35	0.1	0.046	25	0.12	1.40	0.01	0.8	0.09	0.96

Fig. 5 Stress paths followed by a point located at a distance of 37.5 mm from the bottom face (numerical results)
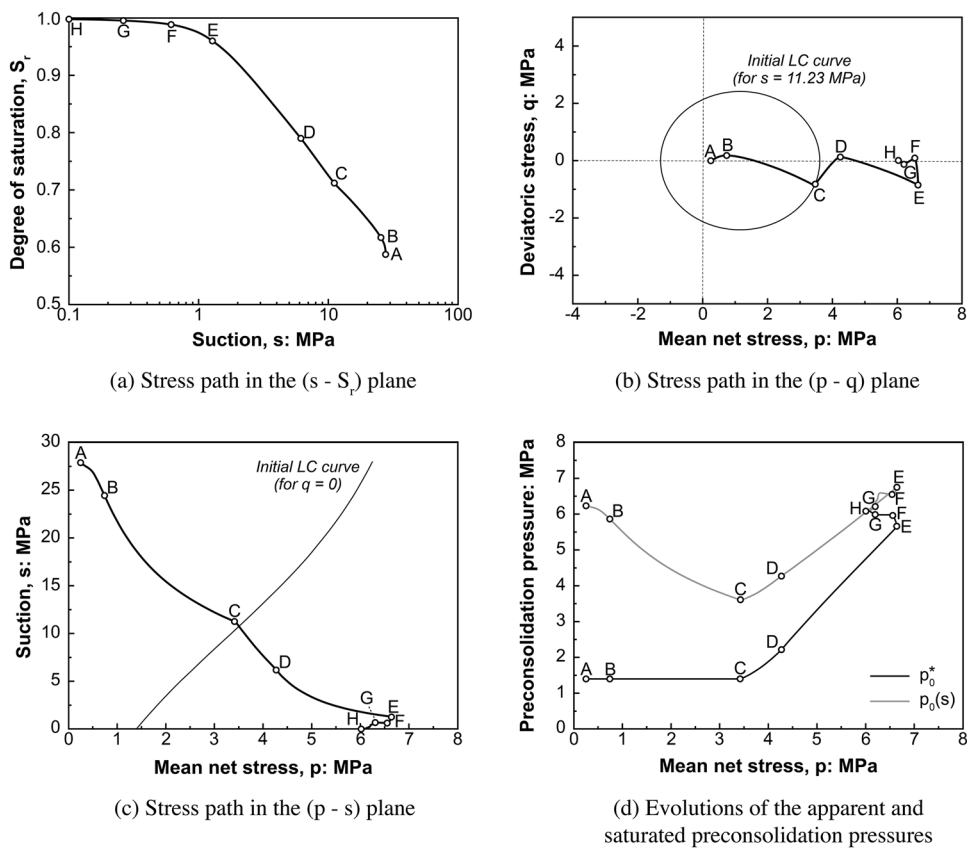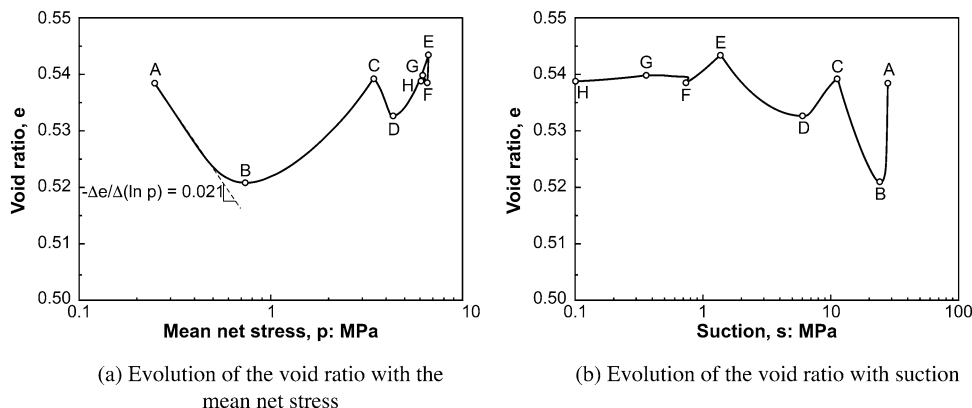

(a) Stress path in the (s - S_r) plane

(b) Stress path in the (p - q) plane

(c) Stress path in the (p - s) plane

(d) Evolutions of the apparent and saturated preconsolidation pressures

Fig. 6 Strain paths followed by a point located at a distance of 37.5 mm from the bottom face (numerical results)

(a) Evolution of the void ratio with the mean net stress

(b) Evolution of the void ratio with suction

strain states moved progressively from A to H according to the following sequence:

(a) **From A to B**: the suction decrease imposed at the bottom of the sample has hardly impacted the considered point (Fig. 5a). However, as a result of hydration and swelling of the lower part of the sample, the vertical stress increases and the point undergoes elastic loading (Fig. 5b). As a result, the void ratio decreases, with a slope in the ($\ln p - e$) plane (=0.021) close to the elastic compressibility (=0.025) (Fig. 6a). In addition, this increase in vertical stress comes with an increase

in deviatoric stress (Fig. 5b). In particular, the slope of the path in the ($p - q$) plane is equal to 0.58, which is hardly lower than the slope of oedometer loading. Finally, the decrease in void ratio at almost constant suction yields an increase in the degree of saturation (Fig. 5a).

(b) **From B to C**: the effects of hydration become prominent and control the compressibility behaviour. The considered point undergoes elastic swelling due to suction decrease. The swelling entails an increase in both void ratio (Fig. 6) and mean net stress (Fig. 5c). Indeed, while swelling is prevented at the global scale

(as a result of the imposed confined conditions), local swelling within the sample is possible. Yet, radially, the sample is not able to swell (the hydration front is assumed to be homogeneous). It yields an increase in radial stress, which becomes higher than the vertical stress, and thus a decrease in the deviatoric stress (Fig. 5b). Finally, since the behaviour is elastic, the preconsolidation pressure for saturated conditions remains constant (Fig. 5d). However, the decrease in suction leads to an important decrease in the apparent preconsolidation pressure and a reduction of the elastic domain.

(c) **C**: the decrease in the apparent preconsolidation pressure is such that the stress path reaches the Loading–Collapse (LC) curve (Fig. 5b). Note that, in Fig. 5c, the LC curve is plotted for a deviatoric stress equal to 0, which is the reason why the point C is apparently not on the yield surface.

(d) **From C to D**: the behaviour is now elastoplastic. While hydration continues (Fig. 5a), plastic collapse is observed and the void ratio at the considered point decreases (Fig. 6b). The vertical stress, hence mean stress, remains increasing as hydration and swelling of the sample proceeds. However, laterally, the stress increases at a lower rate due to collapse, so that the deviatoric stress increases (Fig. 5b). Finally, yielding comes along with hardening of the LC curve and increase in the preconsolidation pressure (Fig. 5d).

(e) **From D to E**: hydration continues and the behaviour is still elastoplastic. However, from point D on, elastic swelling due to suction decrease becomes more important than the plastic collapse and the void ratio increases again (Fig. 6). In addition, the radial stress raises and the deviatoric decreases to become negative.

(f) **E**: the threshold degree of saturation $S_r = 0.96$ is reached and any further decrease in suction does not produce volumetric strain.

(g) **From E to F**: swelling of the upper elements leads to compressive strain at the considered point (Fig. 6). Moreover, the stiffness loss associated with the absence of elastic swelling, yields a decrease in the mean net stress. In Fig. 5d, the difference between the apparent and saturated preconsolidation pressures becomes smaller as suction decreases.

(h) **From F to G**: water is injected from the top side of the sample and hydration of the material proceeds. As a result, the mean effective stress decreases, and the point follows an elastic (unloading) stress path. The saturated preconsolidation pressure is constant, while the apparent preconsolidation stress decreases as suction reduces.

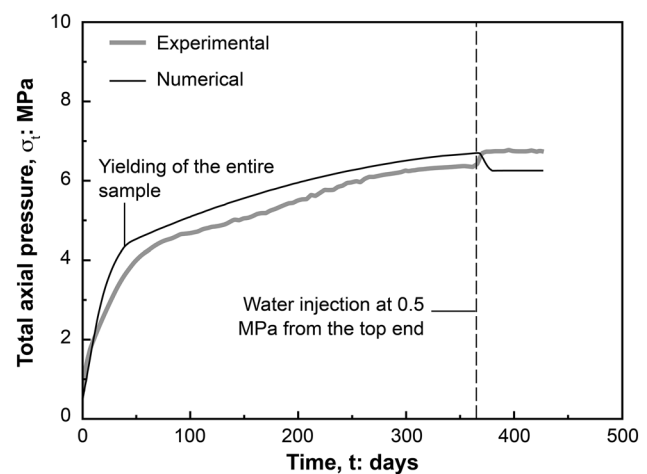(i) **G**: the decrease in the apparent preconsolidation pressure is more important than the decrease in mean stress.

Fig. 7 Total axial pressure. Comparison between experimental data and model predictions

The LC curve is activated once more and the behaviour is elastoplastic.

(j) **From G to H**: hydration of the material proceeds without much volume changes at the considered point.

(k) **H**: the material has reached full saturation at the considered point.

4.3 Total Axial Stress

The evolution of the total axial pressure developed upon hydration is presented in Fig. 7. The development of the vertical swelling pressure exhibited a first stage with a high swelling rate (from the start until day 70 on the experimental curve and day 43 on the numerical one). After that, a significant change of the slope occurred, and a lower swelling rate was observed on both experimental and numerical curves. The numerical simulation can be used to gain a better understanding of the underlying mechanisms. In particular, it shows that hydration of the sample led to a progressive yielding of the material, and that the observed change of swelling rate corresponds to yielding of the entire bentonite sample.

As hydration proceeded and the rate of water intake decreased, a progressive stabilisation of the swelling pressure was observed. After 1 year of water injection, the total vertical pressure developed by the sample was equal to 6.42 MPa, which is in agreement with the swelling pressure determined on smaller samples by Gatabin et al. (2016). Water was then injected from the top end to ensure full saturation of the sample. An increase in the total axial pressure, corresponding approximately to the water injection pressure of 0.5 kPa, was recorded, and the axial pressure reached a

Fig. 8 Total radial pressure along the sample. Comparison between experimental results and numerical predictions

(a) PT1 (y = 12.5 mm)

(b) PT2 (y = 37.5 mm)

(c) PT3 (y = 50.0 mm)

(d) PT4 (y = 75.0 mm)
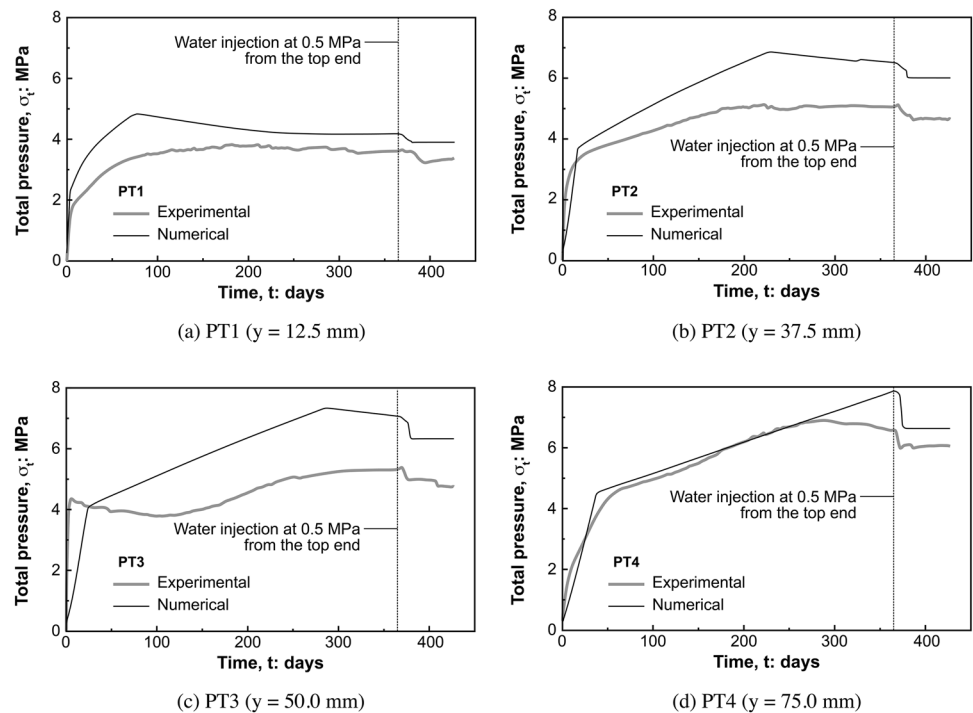
value of 6.75 MPa. On the other hand, the numerical curve shows a decrease in the vertical pressure with stabilisation at 6.26 MPa. This drop of the vertical pressure results from further yielding (pore collapse) of the not-yet fully saturated sample.

4.4 Total Radial Stress

The radial total pressure developed by the sample during hydration was measured at different heights. Fig. 8 compares the experimental and numerical results in terms of total lateral stress. As shown in the figures, the numerical model represents well the experimental data, both qualitatively and quantitatively. The evolution of the radial pressure followed a different trend from the vertical pressure. Although the total radial stress reached after full saturation of the sample was not homogeneous along the sample height, a common trend is observed. The radial pressure was first marked by a rapid elastic increase. Then, the point reached the LC curve and elastoplastic deformations were generated. The curve is marked by a peak corresponding to the reaching of the threshold degree of saturation $S_r = 0.96$. As a consequence of the loss of stiffness, the pressure decreased. After 1 year of hydration from the bottom end, water was injected from the top at 0.5 MPa. Accordingly, the water pressure increased and plastic deformation developed. The total radial pressures exhibited decrease, contrary to the vertical pressure. This decrease is all the more important for sensors close to the top injection front. Finally, the numerical
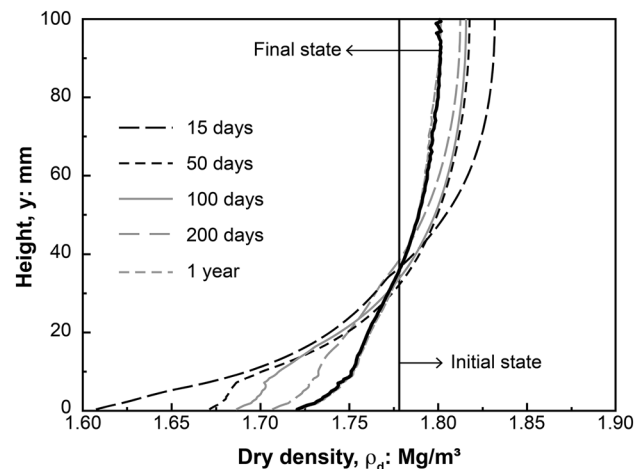

Fig. 9 Evolution over time of the sample dry density (numerical results)

simulations show that full saturation was quickly attained resulting in a stabilisation of the total radial pressures.

4.5 Dry Density Distribution

The numerical simulation provides some insights into the impact of hydration on the sample dry density distribution, while experimental data are not available. Fig. 9 shows that, as soon as hydration started, an important decrease in dry density was observed at the bottom of the sample. Accordingly, the dry density increased in the upper part of
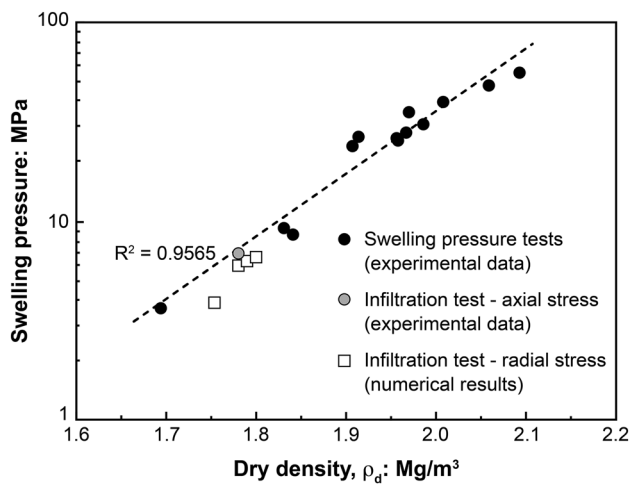
Fig. 10 Comparison between swelling pressure tests performed on small samples (Gatabin et al. 2016) and radial stress predicted by the model

the sample as global swelling of the sample was prevented (swelling at the bottom of the sample yielded compressive strains in the upper part). As hydration proceeded and suction decreased within the sample, elements more and more distant from the wetting end tended to swell, and an important redistribution of the dry density was noticed. However, the development of irrecoverable strains resulting from hydration led to a non-uniform distribution of dry density that persisted at the saturated equilibrated state.

It is worth noting that this conclusion is consistent with other experimental observations made at laboratory scale (Villar et al. 2008; Wang et al. 2013a; Saba et al. 2014b) and field scale (Villar and Lloret 2007). In particular, Wang et al. (2013a) measured relative changes of dry density ranging between -3 and 6% of the initial (and average) value, on the same compacted bentonite–sand mixture saturated under constant-volume conditions.

5 Discussion

The experimental observations and numerical modelling revealed that the progressive and non-uniform hydration of an initially homogeneous bentonite sample led to heterogeneities in both the stress state and density distributions. These heterogeneities evolve during hydration, but persist at the final equilibrated state. In particular, the radial stress varies considerably along the sample height. The evolution of the radial stress was satisfactorily reproduced by the numerical model, without considering possible friction between the sample and the cell wall.

To complement the infiltration test, small-scale (30 mm high) swelling pressure tests were performed on the same

material uniaxially compacted to different dry densities and with different initial water contents (ranging from 7.1 to 12.4%). Samples were then placed in swelling cells and hydrated using a synthetic water representative of the site of Bure. Only the vertical swelling pressure was monitored, using kilogram-accurate load sensors, inserted between the top piston and the upper flange. Fig. 10 shows that the swelling pressure increases exponentially with the dry density. The final radial stress at 12.5, 37.5, 50 and 75 mm from the wetting front of the injection column, as obtained by the numerical model, are also represented as a function of the material dry density at the corresponding height. Interestingly, these points seem to follow the same trend curve as the swelling pressure tests. While the axial pressure measures the overall swelling potential of the sample, the radial stress reflects the local state of the sample.

6 Concluding Remarks

This paper presents a comprehensive experimental and numerical study of the swelling behaviour of isotropically compacted bentonite subjected to hydration under constant-volume conditions. To track the evolution of the mechanical state of the sample during hydration, the axial and radial total stresses at different distances from the wetting end were recorded over time. The experimental data show a complex and non-uniform evolution of the axial and radial stresses over time, as well as anisotropy of the total stresses, which persists at the saturated equilibrated state. In particular, the radial stress appeared to be much lower or higher than the axial stress, depending on the distance from the hydration end.

To help understand the test results, the experimental test was modelled using an advanced hydromechanical framework for partially saturated porous media, accounting for the evolving microstructure of the material. The evolution of the total axial and radial stresses with time is explained by an advancing hydration and swelling front in the bentonite sample, and by the development of irreversible deformations. While the axial stress reflects the overall state of the stress of the sample, the radial stress reveals the local state of the sample. The numerical simulation further showed that, despite the initial sample homogeneity, hydration from one end generated not only inhomogeneities in the stress state, but also in the dry density distribution. This conclusion drawn from the numerical analysis is consistent with other experimental observations for laboratory and field tests (Villar and Lloret 2007; Villar et al. 2008; Wang et al. 2013a; Saba et al. 2014b). Interestingly the relationship between the local dry density and the radial stress seems to follow the global dry density–swelling pressure trend determined on small-scale samples.

Finally, this study highlights the importance of reliable coupled numerical modelling for the design of engineered barriers in deep geological disposal of radioactive waste. In particular, the present study demonstrates that the swelling capacity of bentonite-based materials cannot be characterised by a unique swelling pressure. Reliable predictions for the swelling pressure field within bentonite seals are essential as good contact between the disposal elements should be guaranteed to avoid preferential pathways for radionuclides migration along interfaces. On the other hand, the radionuclide retention capacity and the water and gas permeabilities of bentonites seals, which are key parameters for the safety assessment, strongly depend on the material dry density.

Appendix A

The mechanical model used in this work is an extension of the Barcelona Basic Model proposed by Alonso et al. (1990). The model belongs the family of elastoplastic strain-hardening models and adopts the net stress $\boldsymbol{\sigma}$ and suction s as stress variables. In the elastic domain, the net stress increment is related to the increments of strains and suction through

$$d\boldsymbol{\sigma} = \boldsymbol{D}^e : d\boldsymbol{\varepsilon}^e + \boldsymbol{\alpha}_s ds \tag{A1}$$

where $\boldsymbol{D}^e$ is the global elastic tensor and $\boldsymbol{\alpha}_s$ is the elastic tensor for suction changes, given, respectively, by

$$D^e_{ijkl} = 2G\delta_{ik}\delta_{jl} + \left(K - \frac{2}{3}G\right)\delta_{ij}\delta_{kl} \tag{A2}$$

and

$$\boldsymbol{\alpha}_s = \frac{1}{K_s}\boldsymbol{D}^e : \boldsymbol{I}. \tag{A3}$$

In these equations, K and G are the bulk and shear moduli, given by

$$K = \frac{(1+e)p}{\kappa} \tag{A4}$$

and

$$G = \frac{3(1-2\nu)K}{2(1+\nu)} \tag{A5}$$

with κ, the slope of the unloading–reloading line, e, the void ratio, p, the mean net stress and ν, the Poisson's ratio. K_s is the bulk modulus for changes in suction and is expressed as

$$K_s = \frac{(1+e)(s+u_{atm})}{\kappa_s} \tag{A6}$$

where κ_s is the slope of the reversible wetting–drying line and u_{atm} is the atmospheric pressure.

The elastic domain is bounded by the following yield surface

$$f_{LC} \equiv 3J_2^2 + M_\theta^2(p+p_s)(p-p_0) = 0 \tag{A7}$$

where

- J_2 is the second invariant of the deviatoric stress tensor,
- M_θ is the slope of the critical state line, which depends on the Lode's angle according to van Eekelen (1980) formulation,
- p_s considers the dependence of shear strength on suction and is given by

$$p_s(s) = \frac{c(0) + ks}{\tan\phi} \tag{A8}$$

where $c(0)$ is the cohesion under saturated conditions, k is a parameter controlling the increase in cohesion and ϕ is the friction angle,

- p_0 is the apparent preconsolidation pressure at a suction s according to

$$p_0(s) = p_c\left(\frac{p_0^*}{p_c}\right)^{\frac{\lambda(0)-\kappa}{\lambda(s)-\kappa}} \tag{A9}$$

where p_c is a reference net pressure, p_0^* is the preconsolidation pressure under saturated conditions and $\lambda(s)$ is the slope of the virgin consolidation line, which is a function of suction according to

$$\lambda(s) = \lambda(0)[(1-r)exp(-\omega s) + r] \tag{A10}$$

where r and ω are material parameters, r is related to the maximum stiffness of the soil (for an infinite suction) and ω controls the rate of increase in the soil stiffness with suction.

The formulation of the mechanical model is completed with a non-associated flow rule. The corresponding flow surface is given by
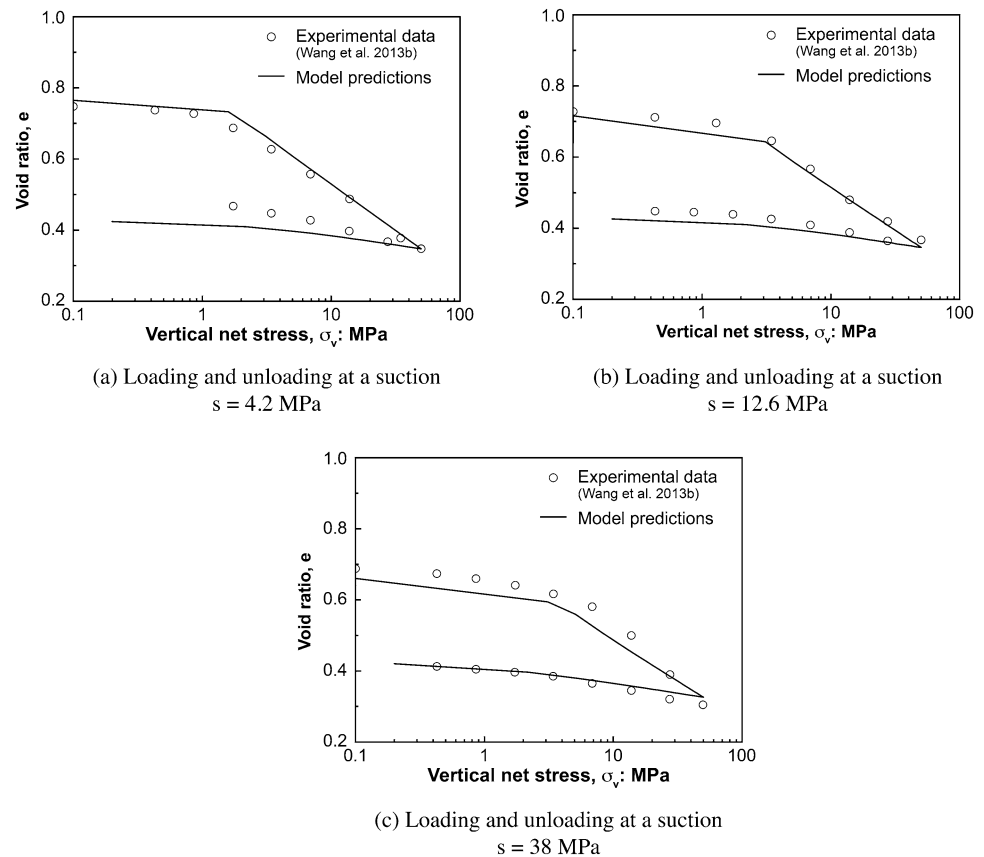
$$g_{LC} \equiv \alpha 3J_2^2 + M_\theta^2(p+p_s)(p-p_0) = 0 \tag{A11}$$

with

$$\alpha = \frac{M_\theta(M_\theta - 9)(M_\theta - 3)}{9(6 - M_\theta)} \frac{1}{1 - \frac{\kappa}{\lambda(0)}}. \tag{A12}$$

The model parameters were calibrated against experimental data from hydration tests under oedometer conditions and controlled-suction oedometer tests from Wang et al. (2013a, b) (Fig. 11).

Fig. 11 Controlled-suction oedometer tests on an MX-80 bentonite/sand mixture compacted at a dry density $\rho_d = 1.67$ Mg/m^3. Calibration of the mechanical model against experimental data (Wang et al. 2013a, b)

(a) Loading and unloading at a suction s = 4.2 MPa

(b) Loading and unloading at a suction s = 12.6 MPa

(c) Loading and unloading at a suction s = 38 MPa

Declarations

Conflict of Interest The authors declare that they have no conflict of interest.

References

Agus SS, Schanz T (2008) A method for predicting swelling pressure of compacted bentonites. Acta Geotech 3:125–137

Agus SS, Arifin YF, Tripathy S, Schanz T (2013) Swelling pressure—suction relationship of heavily compacted bentonite–sand mixtures. Acta Geotech 8(2):155–165

Alonso EE, Gens A, Josa A (1990) A constitutive model for partially saturated soils. Géotechnique 40(3):405–430

Alonso EE, Romero E, Hoffmann C (2011) Hydromechanical behaviour of compacted granular expansive mixtures: experimental and constitutive study. Géotechnique 61(4):329–344

ASTM D4546 (2014) Standard test methods for one-dimensional swell or collapse of soils. American Society for Testing Materials International, West Conshohocken, Pennsylvania, USA

Bernachy-Barbe F (2021) Homogenization of bentonite upon saturation: density and pressure fields. Appl Clay Sci 209:106122

Brackley JJA (1973) Swell pressure and free swell in compacted clay. In: Proceeding of 3rd International Conference on Expansive soils, Haifa 1, 169–176

Bucher F, Müller-Vonmoos M (1989) Bentonite as a containment barrier for the disposal of highly radioactive wastes. Appl Clay Sci 4(2):157–177

Charlier R (1987) Approche unifiée de quelques problèmes non linéaires de mécanique des milieux continus par la méthode des éléments finis (grandes déformations des métaux et des sols, contact

unilatéral de solides, conduction thermique et écoulements en milieu poreux). Ph.D. thesis, Université de Liège

Collin F, Li XL, Radu JP, Charlier R (2002) Thermo-hydro-mechanical coupling in clay barriers. Eng Geol 64:179–193

Cui YJ, Yahia-Aissa M, Delage P (2002) A model for the volume change behavior of heavily compacted swelling clays. Eng Geol 64(2–3):233–250

de La Vaissière R (2013) Hydration versus gas percolation in bentonite. In-situ experiment PGZ2. Experimental borehole results. FORGE Report D3.18, 99 pp

Della Vecchia G, Dieudonné AC, Jommi C, Charlier R (2015) Accounting for evolving pore size distribution in water retention models for compacted clays. Int J Num Anal Methods Geomech 39:702–723

Denis JD (1991) Compaction and swelling of Ca-smectite in water and in $CaCl_2$ solutions: water activity measurements and matric resistance to compaction. Clay and Clay Minerals 39(1):35–42

Dieudonné AC, Della Vecchia G, Charlier R (2017) A water retention model for compacted bentonites. Can Geotech J 54(7):915–925

Dieudonné AC and Charlier R (2017) Evaluation of the instantaneous profile method for the determination of the relative permeability function. Springer Series in Geomechanics and Geoengineering, 181–188

Dieudonné AC, Levasseur S, Charlier R, Della Vecchia G and Jommi C (2013) A water retention model for compacted clayey soils. Computational Geomechanics, COMGEO III - Proceedings of the 3nd International Symposium on Computational Geomechanics: 23–31

Gatabin C, Talandier J, Collin F, Charlier R, Dieudonné AC (2016) Competing effects of volume change and water uptake on the water retention behaviour of a compacted MX-80 bentonite/sand mixture. Appl Clay Sci 121–122:57–62

Harrington JF, Daniel KA, Wisseall AC, Sellin P (2020) Bentonite homogenisation during the closure of void spaces. Int J Rock Mech Min Sci 136:104535

Hicher PY, Wahyudi H, Tessier D (2000) Microstructural analysis of inherent and induced anisotropy in clay. Mech Cohes-Frict Mater 5(5):341–371

Jacinto AC, Villar MV, Ledesma A (2012) Influence of water density on the water-retention curve of expansive clays. Géotechnique 62(8):657–667

Lee JO, Lim JG, Kang IM, Kwon S (2012) Swelling pressures of compacted Ca-bentonite. Eng Geol 129–130:20–26

Lloret A, Villar MV, Sánchez M, Gens A, Pintado X, Alonso EE (2003) Mechanical behaviour of heavily compacted bentonite under high suction changes. Géotechnique 53(1):27–40

Middelhoff M, Cuisinier O, Masrouri F, Talandier J, Conil N (2020) Combined impact of selected material properties and environmental conditions on the swelling pressure of compacted claystone/bentonite mixtures. Appl Clay Sci 184:05389

Olivella S, Carrera J, Gens A, Alonso EE (1994) Non isothermal multiphase flow of brine and gas through saline media. Transp Porous Media 15:271–293

Panday S, Corapcioglu MY (1989) Reservoir transport equations by compositional approach. Transp Porous Media 4:369–393

Pusch R (1992) Use of bentonite for isolation of radioactive waste products. Clay Miner 27(3):353–361

Rao SM, Thyagaraj T (2007) Swell–compression behaviour of compacted clays under chemical gradients. Can Geotech J 44(5):520–532

Rawat A, Baille W, Tripathy S (2019) Swelling behavior of compacted bentonite-sand mixture during water infiltration. Eng Geol 257:10514

Rawat A, Lang L, Baille W, Dieudonné AC, Collin F (2020) Coupled hydro-mechanical analysis of expansive soils: parametric identification and calibration. J Rock Mech Geotech Eng 12(3):620–629

Romero E, Della Vecchia G, Jommi C (2011) An insight into the water retention properties of compacted clayey soils. Géotechnique 61(4):313–328

Roscoe KH and Burland JB (1968) On the generalized stress–strain behaviour of the "wet" clay. In: Heyman J and Leckic F (eds) Engineering plasticity. Cambridge, UK, pp 535–609

Saba S, Barnichon JD, Cui YJ, Tang AM, Delage P (2014a) Microstructure and anisotropic swelling behaviour of compacted bentonite/sand mixture. J Rock Mech Geotech Eng 6(2):126–132

Saba S, Cui YJ, Tang AM, Barnichon JD (2014b) Investigation of the swelling behaviour of compacted bentonite–sand mixture by mock-up tests. Can Geotech J 51(12):1399–1412

Sato H, Suzuki S (2003) Fundamental study on the effect of an orientation of clay particles on diffusion pathway in compacted bentonite. Appl Clay Sci 23(1–4):51–60

Sellin P, Leupin O (2013) The use of clay as an engineered barrier in radioactive-waste management—a review. Clays Clay Miner 61(6):477–498

Sridharan A, Rao AS, Sivapullaiah PV (1986) Swelling pressure of clays. Geotech Test J 9(1):24–33

Sun H, Masin D, Najser J, Nedela V, Navrátilová E (2019) Bentonite microstructure and saturation evolution in wetting—drying cycles evaluated using ESEM, MIP and WRC measurements. Géotechnique 69(8):713–726

Tang AM, Cui YJ (2010) Effects of mineralogy on thermo-hydromechanical parameters of MX80 bentonite. J Rock Mech Geotech Eng 2(1):91–96

Tang AM, Cui YJ, Le TT (2008) A study on the thermal conductivity of compacted bentonites. Appl Clay Sci 41(3–4):181–189

van Eekelen HAM (1980) Isotropic yield surfaces in three dimensions for use in soil mechanics. Int J Numer Anal Meth Geomech 4(1):89–101

Villar MV, Lloret A (2007) Dismantling of the first section of the FEBEX in situ test: THM laboratory tests on the bentonite blocks retrieved. Phys Chem Earth 32:716–729

Villar MV, Lloret A (2008) Influence of dry density and water content on the swelling of a compacted bentonite. Appl Clay Sci 39(1–2):38–49

Villar MV, Sanchez M, Gens A (2008) Behaviour of a bentonite barrier in the laboratory: experimental results up to 8 years and numerical simulation. Phys Chem Earth 33:S476–S485

Villar MV, Gutiérrez-Álvarez C, Campos G (2023) Bentonite swelling into a void under suction or water flow. Acta Geotech 18:1495–1513

Voltolini M, Wenk HR, Mondol NH, Bjorlykke K, Jahren J (2009) Anisotropy of experimentally compressed kaolinite-illite-quartz mixtures. Geophysics 74(1):D13–D23

Wang Q, Tang AM, Cui YJ, Delage P, Gatmiri B (2012) Experimental study on the swelling behaviour of bentonite/claystone mixture. Eng Geol 124:59–66

Wang Q, Cui YC, Tang AM, Barnichon JD, Saba S, Ye WM (2013a) Hydraulic conductivity and microstructure changes of compacted bentonite/sand mixture during hydration. Eng Geol 164:67–76

Wang Q, Tang AM, Cui YJ, Delage P, Barnichon JD, Ye WM (2013b) The effects of technological voids on the hydro-mechanical behaviour of compacted bentonite–sand mixture. Soils Found 53(2):232–245

Zeng G, Cui YJ, Zhang F, Conil N, Talandier J (2020) Effect of technological voids on swelling behaviour of compacted bentonite–claystone mixture. Can Geotech J 57(12):593–660

Zeng G, Cui YJ, Conil N, Talandier J (2022) Effects of technological voids and hydration time on the hydro-mechanical behaviour of compacted bentonite/claystone mixture. Géotechnique 72(1):34–47